



OPEN

Altered structural connectivity in olfactory dysfunction after mild COVID-19 using probabilistic tractography

Diógenes Diego de Carvalho Bispo^{1,2,3,10}✉, Pedro Renato de Paula Brandão^{4,5,10}, Danilo Assis Pereira⁶, Fernando Bisinoto Maluf³, Bruna Arrais Dias³, Hugo Rafael Paranhos³, Felipe von Glehn^{2,5}, Augusto César Penalva de Oliveira⁷, Alexandre Anderson de Sousa Munhoz Soares², Maxime Descoteaux^{8,9,11} & Neysa Aparecida Tinoco Regattieri^{2,11}

We aimed to investigate changes in olfactory bulb volume and brain network in the white matter (WM) in patients with persistent olfactory dysfunction (OD) following COVID-19. A cross-sectional study evaluated 38 participants with OD after mild COVID-19 and 24 controls, including Sniffin' Sticks identification test (SS-16), MoCA, and brain magnetic resonance imaging. Network-Based Statistics (NBS) and graph theoretical analysis were used to explore the WM. The COVID-19 group had reduced olfactory bulb volume compared to controls. In NBS, COVID-19 patients showed increased structural connectivity in a subnetwork comprising parietal brain regions. Regarding global network topological properties, patients exhibited lower global and local efficiency and higher assortativity than controls. Concerning local network topological properties, patients had reduced local efficiency (left lateral orbital gyrus and pallidum), increased clustering (left lateral orbital gyrus), increased nodal strength (right anterior orbital gyrus), and reduced nodal strength (left amygdala). SS-16 test score was negatively correlated with clustering of whole-brain WM in the COVID-19 group. Thus, patients with OD after COVID-19 had relevant WM network dysfunction with increased connectivity in the parietal sensory cortex. Reduced integration and increased segregation are observed within olfactory-related brain areas might be due to compensatory plasticity mechanisms devoted to recovering olfactory function.

Since its discovery in Wuhan, China, in late 2019, coronavirus disease 2019 (COVID-19), caused by severe acute respiratory syndrome coronavirus 2 (SARS-CoV-2), has resulted in more than 600 million infected and 6 million deaths¹ and put unprecedented pressure on social, economic and health systems around the world². While initial research on COVID-19 has focused on acute illnesses, it lately has become clear that long-term consequences occur³. Many survivors of acute infection have persistent and disabling neurological symptoms, which can have socioeconomic and personal consequences. It is, therefore, imperative that there is a thorough understanding of evolving clinical syndromes and underlying pathophysiological mechanisms, allowing rational therapeutic interventions to be implemented quickly².

Olfactory dysfunction has variable severity, including anosmia, hyposmia, and parosmia, and affects 30–70% of patients with COVID-19⁴. It occurs early in the course of infection, with no direct association with disease

¹Diagnostic Imaging Unit, Brasilia University Hospital, University of Brasilia, Darcy Ribeiro Campus, Asa Norte, Brasilia, Distrito Federal, Brazil. ²Faculty of Medicine, University of Brasilia, Brasilia, Distrito Federal, Brazil. ³Department of Radiology, Hospital Santa Marta, Taguatinga, Distrito Federal, Brazil. ⁴Neuroscience and Behavior Lab, University of Brasilia, Brasilia, Distrito Federal, Brazil. ⁵Hospital Sírío-Libanês, Brasilia, Distrito Federal, Brazil. ⁶Advanced Psychometry Laboratory, Brazilian Institute of Neuropsychology and Cognitive Sciences, Brasilia, Distrito Federal, Brazil. ⁷Department of Neurology, Instituto de Infectologia Emílio Ribas, São Paulo, Brazil. ⁸Sherbrooke Connectivity Imaging Lab, University of Sherbrooke, Sherbrooke, QC, Canada. ⁹Imeka Solutions Inc, Sherbrooke, QC, Canada. ¹⁰These authors contributed equally: Diógenes Diego de Carvalho Bispo and Pedro Renato de Paula Brandão. ¹¹These authors jointly supervised this work: Maxime Descoteaux and Neysa Aparecida Tinoco Regattieri. ✉email: dbispo.neurorradio@gmail.com

severity or viral burden⁵. In one study, hyposmia was the first clinically presenting symptom in around 12% of patients⁶. In most cases, recovery is spontaneous within 3 to 4 weeks^{5,7}. However, some patients develop persistent olfactory impairment up to 12 months after infection, suggesting that the damage to the olfactory system may be severe or permanent⁵.

Several hypotheses were proposed to explain the underlying mechanism for olfactory dysfunction in COVID-19^{8,9}. The most notable theory regarding COVID-related hyposmia is the direct infection of olfactory receptor neurons by SARS-CoV-2 through the nasal mucosa. However, there is conflicting evidence on whether SARS-CoV-2 can indeed infect these neurons¹⁰. Angiotensin-converting enzyme 2 receptors—the target molecules for SARS-CoV-2, are not expressed in neural cells but by non-neuronal support cells in the olfactory epithelium. The lack of direct neuronal damage could justify the rapid recovery of olfactory function in most patients¹¹. Despite this, SARS-CoV-2 infection seems to generate axonal pathology and microvasculopathy in the olfactory bulbs and tracts in those with olfactory alterations, due to local inflammation¹².

Olfactory dysfunction during or after COVID-19 represents a marker of neurological disease and can be assessed with olfactory nerve imaging. Magnetic resonance imaging (MRI) can help evaluate patients with anosmia and hyposmia because it allows for elaborate visualization and measurement of the olfactory anatomical structures. Yet, studies that describe MRI-based anatomical changes in olfactory structures in COVID-19 are sparse and mainly represented by case reports. Despite this, a reduction in olfactory bulbs was described in 36 participants who had COVID-19 olfactory dysfunction compared to a control group 2 to 8 weeks after infection¹³, and in 196 subjects who had COVID-19 compared to controls 1 to 582 days after disease onset¹⁴. The association between olfactory bulb atrophy and severity of the olfactory dysfunction was not evaluated in these studies. Furthermore, the impact on brain connections is relatively unknown, especially in sensory and olfactory-related regions.

Diffusion-weighted magnetic resonance imaging (dMRI)-derived tractography is an advanced technique that may be used to investigate the mechanisms underlying anosmia by reconstructing major brain fiber pathways. This method allows for the mapping of white matter (WM) pathways through voxel-wise fiber orientations. It enables the reconstruction of structural connectivity matrices, generating networks that represent parts or the whole brain's anatomical organization, with streamlines serving as proxies for WM fiber bundles¹⁵. The Convex Optimization Modeling for Microstructure Informed Tractography 2 (COMMIT2) framework is used to remove false positive brain connections by assigning to each streamline its contribution to the dMRI signal, while imposing an anatomical regularization encouraging streamlines to group together as bundles in the connectivity matrix^{16,17}. This filtering method significantly improves the accuracy of the resulting structural connectomes, thereby enhancing the reliability of the findings¹⁸.

Graph analysis is used to explore changes in the WM network based on graph theory¹⁸. After defining the nodes and edges (connections between regions), graph theory metrics represent distinct aspects of global or local network connectivity. A small-world architecture, for instance, indicates that the minimum path length between any pair of nodes is approximately equivalent to a comparable random network, but the network nodes have greater local interconnectivity or cliquishness than a random network¹⁵. The relationship between olfaction and brain network metrics is intimate. Studies have shown that hyposmia in aging and neurodegeneration relates to WM disconnection using graph analysis methods^{19,20}, whereas individuals with the highest olfactory abilities, such as *sommeliers*, exhibit increased functional network connectivity and higher small-world topology than controls²¹. However, there is still a need for further exploration of WM network changes in non-neurodegenerative hyposmia. The use of graph theory in understanding changes in the WM network may help elucidate the underlying mechanisms of olfactory dysfunction.

The current study used a cross-sectional design to examine changes in the olfactory bulb volume and investigate brain networks in patients after COVID-19 compared to a control group. Our secondary objective was to determine whether there was an association between olfactory bulb volume, structural connectivity measures, and olfactory performance.

Results

Demographic and clinical characteristics. In this study, we recruited a total of 67 individuals, out of which three participants from the COVID-19 group (COV+) were excluded. Two of the exclusions were due to MRI contraindications, while the third exclusion was due to a Montreal Cognitive Assessment (MoCA) score of less than 15. In addition, two participants from the control group (COV-) were excluded from the study. One exclusion was due to a positive SARS-CoV-2 IgG test result, while the other exclusion was due to the detection of a brain structural change on MRI. These exclusions were necessary to ensure the integrity and validity of the data obtained from the study population.

Clinical examinations, cognitive tests, and MRI were administered to a total of 62 participants, comprising 38 in the COV+ group and 24 in the COV- group. The groups did not exhibit any significant differences in age ($p = 0.520$), sex ($p = 0.550$), education ($p = 0.555$), or comorbidity profiles (Table 1). The average time between COVID-19 diagnosis and study's clinical/imaging procedures was 91.7 (± 26.0) days, with a range of 31 to 167 days. No subjects in the COV+ group required hospitalization during the acute phase or thereafter.

There was a significant difference between the two groups in the Sniffin' Sticks smell identification test (SS-16) score ($p < 0.001$). In the COV+ group, 50% of patients were hyposmic (SS-16 test score below 12)²². None of the subjects in the COV- group had hyposmia. MoCA scores did not differ between groups ($p = 0.663$) (Table 1).

Assessment of the olfactory bulbs. The olfactory bulbs of 53 participants (33 in the COV+ group and 20 in the COV- group) were manually segmented. Nine participants were excluded due to movement or magnetic susceptibility artifacts, usually due to metallic material in the oral cavity. In the assessment of interobserver

Demographic and clinical characteristics	COVID-19 (COV +)	Control (COV -)	Statistic
	(n = 38, 61%)	(n = 24, 39%)	
Age	36.4 ± 9.5 (20, 56)	39.3 ± 12.9 (22, 60)	U = 411; p = 0.520 ¹
Sex			
Male, n (%)	10 (26.3%)	8 (33.3%)	$\chi^2 = 0.35$; p = 0.550 ²
Female, n (%)	28 (73.7%)	16 (66.7%)	
Years of formal education	15.1 ± 3.2 (11, 24)	15.5 ± 3.0 (11, 20)	U = 415; p = 0.555 ¹
Comorbidities, n (%)			
Hypertension	3 (7.9%)	0 (0.0%)	$\chi^2 = 0.199$; p = 0.160 ²
Diabetes mellitus	2 (5.3%)	1 (4.2%)	$\chi^2 = 0.04$; p = 0.840 ²
Obesity	1 (2.6%)	1 (4.2%)	$\chi^2 = 0.11$; p = 0.740 ²
Asthma/COPD	2 (5.3%)	2 (8.3%)	$\chi^2 = 0.23$; p = 0.630 ²
Allergic rhinosinusitis	11 (28.9%)	8 (33.3%)	$\chi^2 = 0.13$; p = 0.720 ²
Thyroid disorder	2 (5.3%)	1 (4.2%)	$\chi^2 = 0.04$; p = 0.840 ²
Mood disorder	4 (10.5%)	2 (8.3%)	$\chi^2 = 0.08$; p = 0.780 ²
Migraine	12 (31.6%)	7 (29.2%)	$\chi^2 = 0.04$; p = 0.840 ²
Sniffin' Sticks identification test (SS-16)	11.4 ± 2.1 (6, 15)	13.6 ± 1.1 (12, 16)	U = 177; p < 0.001 ¹
Montreal Cognitive Assessment (MoCA)	24.9 ± 3.2 (17, 30)	25.2 ± 3.4 (17, 30)	U = 426; p = 0.663 ¹

Table 1. Demographic and clinical features (COV + and COV - groups). COPD chronic obstructive pulmonary disease. Data are shown as mean ± standard deviation (minimum, maximum) or n (%). ¹Mann-Whitney U test. ²Chi-square test.

agreement for manual segmentation of the olfactory bulbs, Pearson's correlation coefficients were $r = 0.877$ for the right olfactory bulb and $r = 0.900$ for the left olfactory bulb (two-tailed, $p < 0.001$). The mean and standard deviation of the Dice similarity coefficient (DSC) for right and left olfactory bulbs were 0.815 ± 0.0354 and 0.794 ± 0.0483 , respectively, indicating a good agreement between examiners.

The volume of the right ($t = -4.19$, $p < 0.001$), left ($t = -4.42$, $p < 0.001$), and both ($t = -4.42$, $p < 0.001$) olfactory bulbs was significantly reduced in the COV + group when compared to the COV - group (Table 2). This reduction in the normalized total olfactory bulb volume remained even after controlling for the sex, age, and allergic rhinosinusitis ($F = 17.19$, $p < 0.001$) (Fig. 1A). In the COV + group, there was no difference in normalized total olfactory bulb volume between participants with $SS-16 < 12$ and $SS-16 \geq 12$ ($p = 1.000$, Bonferroni correction). The normalized total olfactory bulb volume was smaller in these COV + subgroups compared to the COV - group (Fig. 1B).

A positive correlation was found between total olfactory bulb volume and SS-16 test performance in the study sample ($n = 53$) ($\rho = 0.281$, $p = 0.014$). In the control group, there was a positive association between the volume of the olfactory bulbs and the SS-16 test score ($\rho = 0.706$, $p = 0.003$) (Fig. 1C). In the COV + group, there was no association between the volume of the olfactory bulbs and the total score of the SS-16 test score ($\rho = 0.009$, $p = 0.964$) (Fig. 1D).

Voxel-based diffusion imaging analysis. No between-group differences were observed for fractional anisotropy (FA), mean diffusivity (MD), radial diffusivity (RD), and axial diffusivity (AD) using Tract-based Spatial Statistics (TBSS), controlling for age and sex ($p > 0.05$).

Network-based statistics (NBS). Using a whole-brain exploratory analysis, NBS identified significant differences in structural connectivity between the COV + and COV - groups. Compared to the control group, COVID-19 patients exhibited significantly higher structural connectivity in a subnetwork composed of three brain regions (one on the right side and two on the left side) and two interhemispheric connections (threshold value $t = 3.0$, $p < 0.05$) (Fig. 2, Supplementary Table S1).

Measure	COVID-19 (COV +)	Control (COV -)	Statistic ¹	Adj p ²
	(n = 33, 62%)	(n = 20, 38%)		
Right olfactory bulb volume (mm ³)	32.2 (9.5)	43.2 (8.8)	$t = -4.19$; $p < 0.001$	$p < 0.001$
Left olfactory bulb volume (mm ³)	31.0 (9.4)	43.1 (10.2)	$t = -4.19$; $p < 0.001$	$p < 0.001$
Total olfactory bulb volume (mm ³)	63.2 (18.4)	86.3 (18.4)	$t = -4.42$; $p < 0.001$	$p < 0.001$

Table 2. Comparison of the olfactory bulb volume between COV + and COV - groups. All data are shown as mean (standard deviation). ¹Independent sample t-test. ²Adjusted p value for FDR.

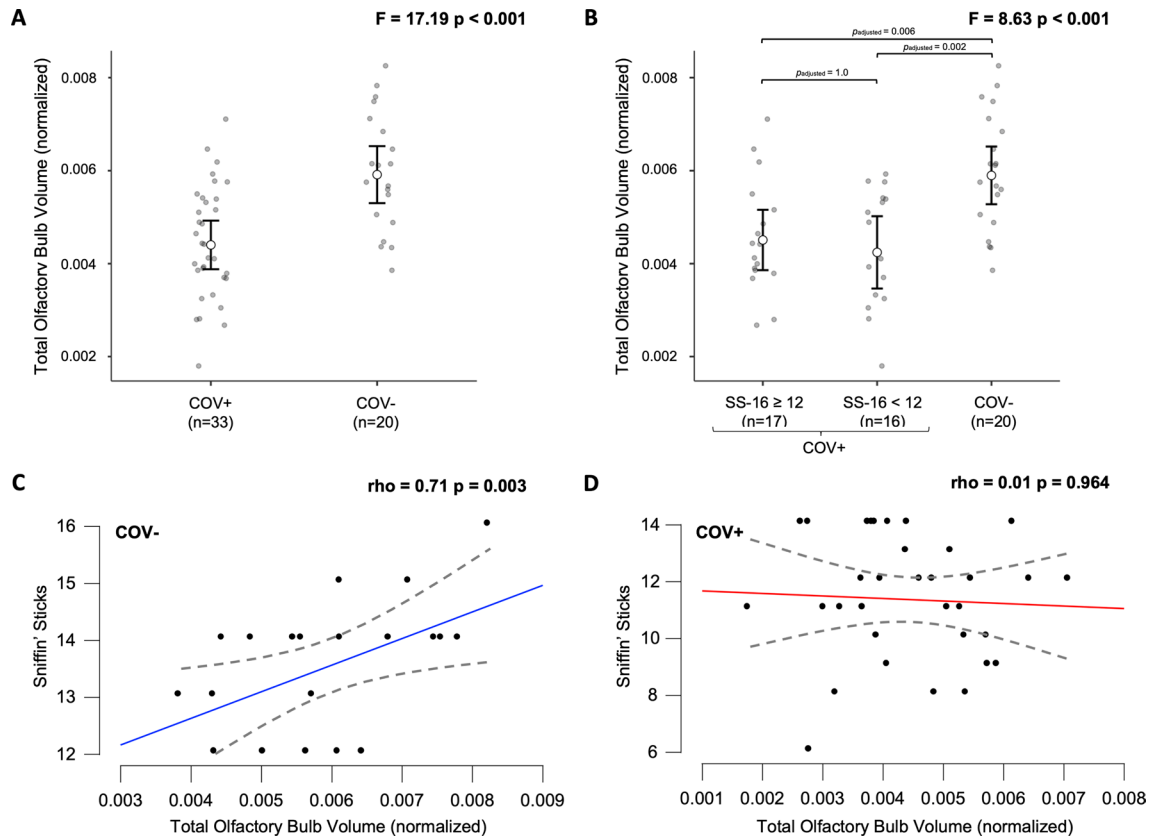


Figure 1. (A) Comparison of the normalized total olfactory bulb volume between the COV– and COV + groups using ANCOVA. (B) Comparison of the normalized total olfactory bulb volume among the COV–, COV + with SS-16 \geq 12 and COV + with SS-16 < 12 subgroups using ANCOVA. (C) Association between normalized total olfactory bulb volume and SS-16 test score in the COV– group. (D) Association between normalized total olfactory bulb volume and SS-16 test score in the COV + group. SS-16 Sniffin' Sticks smell identification test, ANCOVA analysis of covariance. *ANCOVA with covariates including sex, age, and allergic rhinosinusitis.

Graph theory analysis: global network. COV + group showed lower global efficiency ($p=0.019$) and local efficiency ($p=0.047$) and higher assortativity ($p=0.027$) than COV– group. No significant differences were found in other global network metrics ($p>0.05$) (Table 3). Both groups had $\sigma > 1$, which means they satisfied the criteria of a small-world (Table 3). In the COV + group, there was an association between the clustering and the SS-16 test score ($\rho = -0.457$, $p=0.019$), controlling for sex, age, education, comorbidities, and time between COVID-19 diagnosis and study clinical/imaging procedures. No association was identified between global network measures and the SS-16 test score in the COV– group.

Graph theory analysis: local network. Compared with controls, patients exhibited reduced local efficiency (left lateral orbital gyrus and pallidum), increased clustering (left lateral orbital gyrus), increased nodal strength (right anterior orbital gyrus), and reduced nodal strength (left amygdala) after adjusting for multiple comparisons (Table 4, Supplementary Fig. S1).

Discussion

Our study findings reveal that patients with persistent subjective hyposmia following COVID-19 infection exhibited a 25% reduction in olfactory bulb volume at a mean follow-up of three months. In comparison to controls, SARS-CoV-2 infected hyposmic subjects demonstrated significant aberrations in the WM network, but no changes TBSS. The NBS analysis identified a subnetwork in the parietal sensory areas with increased connectivity. The global and local network topological properties demonstrated reduced integration and increased segregation, including olfactory-related brain areas (pallidum, amygdala, and orbitofrontal gyrus). Moreover, the SS-16 test score was negatively correlated with clustering in the COVID-19 group. Therefore, we hypothesize that changes in connectivity in the parietal sensory regions and olfaction-related brain areas may be due to compensatory plasticity mechanisms aimed at restoring olfactory function.

Unlike other upper respiratory infections, COVID-19 olfactory dysfunction is not associated with nasal discharge and conductive obstruction of the olfactory cleft, suggesting a neurological origin²³. SARS-CoV-2 does not infect the sensory neurons, and sustentacular cells are the primary target of this virus in the olfactory mucosa^{10,24–27}. Several studies have also reported changes in olfactory bulb volume, olfactory cleft volume,

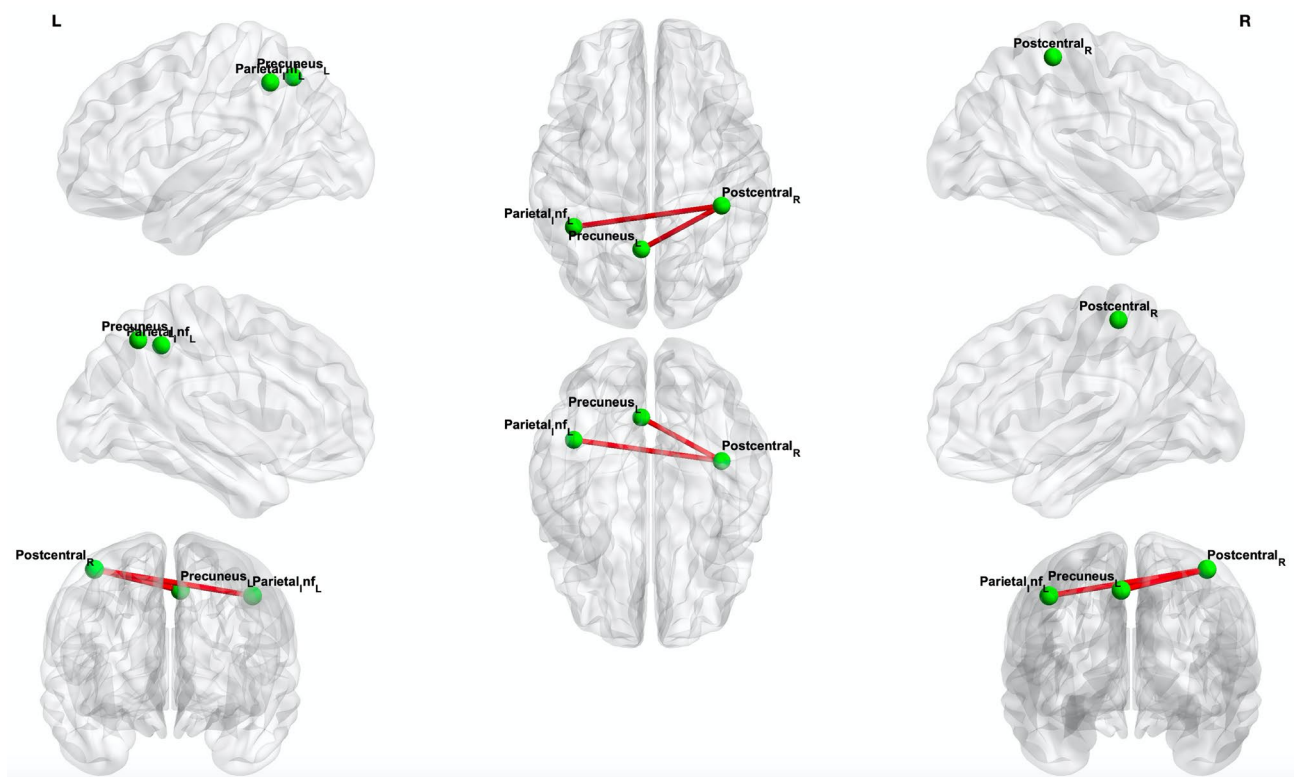


Figure 2. Whole-brain network-based statistics results. The connectivity analysis with threshold value $t = 3.0$ showed a subnetwork with greater connectivity in the COV+ group compared to the COV- group (red edges). Significance was thresholded at $p < 0.05$. Permutations = 5000. *Inf* inferior, *R* right, *L* left.

Measure	COVID-19 (COV+)	Control (COV-)	Statistic	Cohen's d
	(n = 32, 59%)	(n = 22, 41%)		
Betweenness centrality	0.00760 (0.00027)	0.00765 (0.00023)	$t = -0.695$; $p = 0.490^1$	–
Modularity	0.588 (0.577, 0.591)	0.585 (0.580, 0.590)	$U = 327$; $p = 0.669^2$	–
Assortativity	0.01751 (0.0181)	0.00696 (0.0147)	$t = 2.271$; $p = 0.027^{1*}$	0.629
Participation	0.248 (0.0111)	0.247 (0.0115)	$t = 0.532$; $p = 0.597^1$	–
Clustering	1.18 (1.14, 1.25)	1.14 (1.09, 1.19)	$U = 263$; $p = 0.120^1$	–
Nodal strength	91.1 (86.5, 92.0)	89.7 (88.4, 91.3)	$U = 329$; $p = 0.694^2$	–
Local efficiency	49.8 (2.36)	51.2 (2.86)	$t = -2.031$; $p = 0.047^{1*}$	-0.562
Global efficiency	39.1 (1.96)	40.6 (2.55)	$t = -2.413$; $p = 0.019^{1*}$	-0.668
Density	0.147 (0.006)	0.150 (0.007)	$t = -1.808$; $p = 0.076^1$	–
Path length	97.4 (3.77)	98.7 (5.23)	$t = -1.046$; $p = 0.300^1$	–
Edge count	2.40 (0.0422)	2.40 (0.0421)	$t = -0.268$; $p = 0.790^1$	–
Omega	-0.0266 (0.0244)	-0.0205 (0.0202)	$t = -0.966$; $p = 0.339^1$	–
Sigma	1.47 (0.0491)	1.45 (0.0703)	$t = 1.281$; $p = 0.206^1$	–

Table 3. Comparison of global network metrics between the COV+ and COV-. Modularity, clustering, and nodal strength are shown as median (interquartile range). The other variables are shown as mean (standard deviation). ¹Independent sample t-test. ²Mann-Whitney U test. * $p < 0.05$.

olfactory sulcus depth, and olfactory nerve morphology²⁸. In our study, the COVID-19 olfactory bulb volume was significantly smaller than that of the control group, even after accounting for head size.

In the control group, olfactory bulb volume showed a significant positive correlation with olfactory function, even after controlling for confounding variables, which is consistent with prior research²⁹. However, this correlation was not observed in patients with COVID-19. There are several hypotheses that could explain this absence of correlation. Firstly, many individuals who experienced anosmia or hyposmia during the acute phase of COVID-19 eventually recovered their olfactory function⁵. This restoration could be due to the rapid regeneration of the supporting cells in the olfactory nerve from stem cells³⁰. In addition, there is evidence that SARS-CoV-2

Tract	N	Right Hemisphere			Left Hemisphere		
		statistic	p-value	adj p	statistic	p-value	adj p
Betweenness centrality							
Lateral orbital gyrus	54	0.482	0.632	ns	- 2.314	0.025	ns
Insula	54	- 0.826	0.412	ns	- 2.100	0.041	ns
Anterior cingulate cortex (supra)	54	0.916	0.364	ns	- 2.044	0.046	ns
Clustering							
Lateral orbital gyrus	54	- 0.102	0.919	ns	3.344	0.002	0.006
Insula	54	2.213	0.031	ns	- 0.518	0.607	ns
Edge count							
Anterior cingulate cortex (pre)	54	2.061	0.044	ns	- 2.576	0.013	0.049
Local efficiency							
Lateral orbital gyrus	54	- 0.664	0.510	ns	- 2.824	0.007	0.025
Hippocampus	54	- 1.024	0.311	ns	- 2.139	0.037	ns
Putamen	54	- 1.287	0.204	ns	- 2.063	0.044	ns
Pallidum	54	- 1.398	0.168	ns	- 2.532	0.014	0.049
Anterior cingulate cortex (supra)	54	- 1.861	0.069	ns	- 2.187	0.033	ns
Nodal strength							
Anterior orbital gyrus	54	2.477	0.017	0.037	1.781	0.081	ns
Lateral orbital gyrus	54	- 0.784	0.436	ns	2.070	0.044	ns
Amygdala	54	0.555	0.581	ns	- 2.703	0.009	0.028
Anterior cingulate cortex (sub)	54	0.713	0.479	ns	2.096	0.041	ns
Nucleus accumbens	54	- 1.639	0.107	ns	- 2.106	0.040	ns
Path length							
Anterior cingulate cortex (pre)	54	- 0.182	0.856	ns	- 2.241	0.029	ns
Participation							
Insula	54	0.536	0.594	ns	- 2.507	0.015	ns

Table 4. Comparison of local network metrics between the control and COVID-19 groups, adjusting for multiple comparisons (FDR). Age and sex were included as covariates. *Supra* supracallosal, *sub* subgenual, *pre* pregenual, *ns* not significant, *adj* adjusted. Significant p values < 0.05 are indicated in bold font.

can affect WM and gray matter (GM), even in subjects with mild symptoms without hospitalization, which can impact higher processing in brain regions related to the olfactory system^{31–33}.

Reduced global and local efficiency was observed in COV + group, including the olfactory-related regions, compared to the COV- group indicating potential disruption in brain network connectivity. Consistent with these findings, a longitudinal imaging study using UK Biobank data revealed a significant detrimental effect of SARS-CoV-2, mainly on the limbic and olfactory cortical system, as well as changes in diffusion measures in regions functionally connected to the piriform cortex, olfactory tubercle, and anterior olfactory nucleus. Moreover, in that study, participants infected with SARS-CoV-2 showed a more pronounced reduction of grey matter thickness in the left parahippocampal gyrus and lateral orbitofrontal cortex³¹. In other studies, WM microstructural alterations were also observed in the brain during the subacute, post-acute, and chronic phases of COVID-19^{32–34}, with the potential to disrupt brain network connectivity.

Cerebral plasticity after a sensory loss has been well documented in respect of visual and auditory loss, but less is known about the effects of olfactory input loss on the adult brain. Previous research has demonstrated that acquired anosmia alters GM volume or density in olfactory-related areas, such as the piriform cortex and the orbitofrontal cortex, as well as in non-olfactory-related areas, such as the prefrontal cortex. The higher assortativity in the COV + group suggests that the network nodes are more interconnected with nodes that have comparable properties, which may reflect a compensatory mechanism in response to the disruption of brain network connectivity caused by COVID-19. Our study also showed increased structural connectivity in the posterior parietal cortex, involving multisensory areas such as the postcentral gyrus, inferior parietal gyri, and precuneus, in whole-brain analysis. In a functional study, elevated brain connectivity between the orbitofrontal cortex and the visual association cortex and fusiform gyrus in the COVID-19 anosmia group was identified¹⁴. One could hypothesize that the absence of olfactory input to these parietal multisensory areas alters the neuronal constellation and promotes a more efficient multisensory-based integration of visual and auditory perception in anosmic individuals³⁵.

A recent study on patients with olfactory dysfunction following COVID-19 revealed an increased functional intranetwork connectivity within the default mode network, as well as greater internetwork connectivity between the olfactory and default mode networks. This suggests that the compensatory mechanism of greater intranetwork functional connectivity may help to address the deficits in olfactory processing and overall well-being in COVID-19 patients³⁶. In another study, structural and functional connectivity metrics were significantly increased in individuals previously infected with SARS-CoV-2. Greater residual olfactory impairment was associated with

more segregated processing in regions functionally connected to the anterior piriform cortex³⁷. Similarly, we evidenced an increase in segregation in the orbitofrontal cortex and identified a negative correlation between clustering of whole-brain WM and the olfactory test in the COVID-19 group, which was not observed in the control group.

The present study has some limitations that should be acknowledged. Firstly, this was a cross-sectional study with a non-probabilistic sample, which may limit the generalizability of the findings. Additionally, patients were evaluated only once during the post-acute phase, and there was no serial evaluation at different time points, precluding inferences about the temporal dynamics of abnormalities in the olfactory bulbs and WM. Furthermore, the diffusion parameters selected (e.g., low *b*-values) may have limited the quantitative diffusion analysis, although they better reflect the clinical protocol context.

In summary, our study highlights the presence of reduced olfactory bulb volume and WM structural network disruption in patients with persistent hyposmia after COVID-19. Our findings suggest that compensatory mechanisms in the parietal sensory and olfactory-related areas may help alleviate the deficiency in olfactory processing in COVID-19 patients. While larger brain connectivity studies are needed to confirm these observations, longitudinal analyses are particularly important to assess the long-term neurological consequences of COVID-19. Further research is also required to explore the potential impact of olfactory dysfunction on quality of life and daily functioning.

Methods

Participants. This cross-sectional prospective analytical study was conducted as part of the Neuro-COVID-19 Brazilian Registry (NeuroCovBr, <https://www.neurocovbr.com/>)³⁸, between October 2020 and May 2021 in Brasilia, Brazil. Participants were recruited with a non-probabilistic sampling strategy from a population of health professionals and patients assisted at the Brasilia University Hospital before the implementation of mass vaccination campaigns. We consecutively contacted a list of 364 patients diagnosed with COVID-19 by real-time quantitative reverse transcription polymerase chain reaction (qRT-PCR) to invite them to the study.

The inclusion criteria for the COVID-19 group (COV+) were: (a) diagnosis of SARS-CoV-2 infection confirmed by detection of viral RNA by qRT-PCR testing of a nasopharyngeal swab, without requiring hospitalization during infection, (b) COVID-19-related persistent subjective hyposmia, and (c) age between 18 and 60 years old. Patients were evaluated at least four weeks after the diagnosis of COVID-19 to ensure that the acute phase had already passed. The control group (COV-) was recruited from the same population (patients or health professionals from Brasilia University Hospital) using convenience sampling, with age, sex, and education level matched to the COV+ group. Subjects in the COV- group had not been previously infected with SARS-CoV-2, had a negative SARS-CoV IgG/IgM test, and had no olfactory dysfunction.

The exclusion criteria for both groups included (a) pre-existing brain structural disorders (e.g., stroke, epilepsy, multiple sclerosis, neoplasia, hydrocephalus, traumatic brain injury, Parkinson's disease, and dementia), (b) severe psychiatric diseases, (c) MoCA global score of less than 15³⁹, (d) MRI contraindications, and (e) illiteracy.

This study was approved by the local ethics committee at the University of Brasilia and adhered to current regulations, such as the Helsinki Declaration. All participants provided written informed consent and underwent clinical, cognitive, and MRI examinations during the same visit.

Clinical assessment. Demographic and clinical data were collected using electronic forms, including evaluation of neurological, chemosensory, respiratory, and constitutional symptoms. In addition, demographic variables such as age, education, sex, and a list of self-reported comorbidities were obtained.

The Sniffin' Sticks smell identification test (SS-16) was used to evaluate participants' ability to identify odors. This psychophysical test was developed by Burghardt⁴⁰ (Wedel, Germany) and previously adapted to Brazilian Portuguese^{26,27}. The test comprises 16 pens containing common and recognizable odorants. The length of each pen is 14 cm (approximately 5.51 in), with an internal diameter of 1.3 cm (about 0.51 in) and a 4 mL cap containing odorless or odorous liquids dissolved in propylene glycol. The participant had to identify the odor using a four-option forced-choice paradigm.

All participants also responded to a cognitive test, MoCA, to screen for cognitive impairment^{39,40}. It is a brief 30-point test that assesses attention, executive functions, memory, language, visuoconstructional skills, conceptual thinking, and calculations.

MRI data acquisition. The MRI was performed using a Philips Achieva 3 T scanner (Best, Netherlands) equipped with an 8-channel SENSE coil. The following MRI sequences were obtained: (1) Three dimensional (3D) T1-weighted sequence, turbo field echo (TFE), sagittal, with field of view (FOV) = 208 × 240 × 256 mm, reconstructed resolution of 1 × 1 × 1 mm, echo time (TE) = min full echo, repetition time (TR) = 2300 ms, TI = 900 ms, two times accelerated acquisition; (2) Diffusion-weighted sequence, axial, with FOV 232 × 232 × 160 mm, reconstructed resolution of 2 × 2 × 2 mm, TE = 71 ms; TR = 3300 ms, 32 directions (*b* = 800 s/mm²); (3) Diffusion-weighted sequence, axial, with FOV 232 × 232 × 160 mm, reconstructed resolution of 2 × 2 × 2 mm, TE = 71 ms; TR = 3300 ms (reversed phase encoded b0); (4) 3D-fluid attenuated inversion recovery (FLAIR) sequence, sagittal, with FOV 256 × 256 × 160 mm, reconstructed resolution of 1.2 × 1 × 1 mm, TE = 119 ms, TR = 4800 ms, TI = 1650 ms. (5) T2-weighted sequence, coronal, with FOV 264 × 204 mm, reconstructed resolution of 0.25 × 0.25 × 1.5 mm, TR = 2500 ms, TE = 80 ms; flip angle = 90, with coverage of the anterior cranial fossa.

Manual segmentation of the olfactory bulbs. Two independent evaluators blinded to clinical and olfactory data manually segmented the volumes of the olfactory bulbs using ITK-SNAP (version 3.8) (Fig. 3)⁴¹. The limits of the olfactory bulb in the coronal plane were determined by the surrounding cerebrospinal fluid,

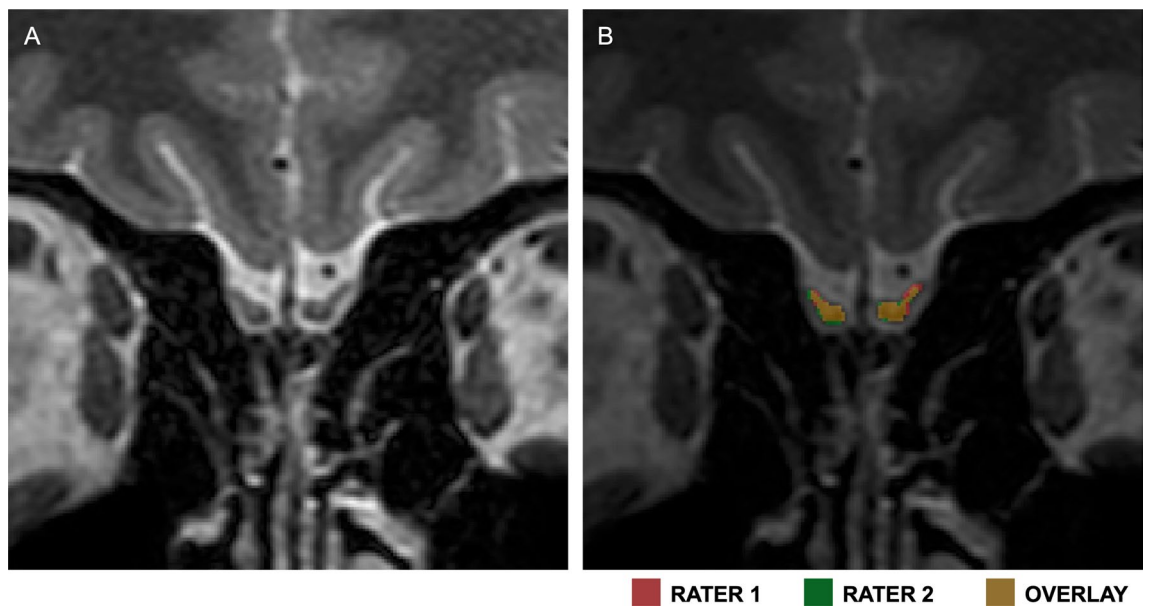


Figure 3. Manual segmentation of the olfactory bulbs. A. Coronal T2-weighted image of a participant. B. Coronal T2-weighted image with segmentations made by the two evaluators. Red: Rater 1; Green: Rater 2; Yellow: Overlap.

while an abrupt diameter change defined the posterior boundary of the olfactory bulb at the transition with the olfactory tract⁴². The volumetric measures of the right and left olfactory bulbs were taken independently and then summed. The mean values established by the two evaluators were used in all subsequent analyses. Interobserver agreement was evaluated using Pearson's correlation coefficient and the DSC (Fig. 3).

The estimated total intracranial volume (eTIV) was computed using FreeSurfer (version 7.1.1, <http://surfer.nmr.mgh.harvard.edu>) which normalized the volumes of the olfactory bulbs to eliminate biases caused by unequal head sizes.

Diffusion magnetic resonance imaging processing. TractoFlow was used to analyze dMRI and T1-weighted images (Fig. 4)⁴³. As an automated tool for processing dMRI, it extracts diffusion tensor imaging (DTI) measures. FA, MD, RD, and AD were calculated. Probabilistic whole-brain anatomically constrained particle filtering tractography was performed on a fiber orientation distribution function (fODF) of maximum spherical harmonics order of 6⁴⁴. The output of TractoFlow was then further processed via advanced steps to generate structural connectomes using SCILPY library version 1.0.0⁴⁵. Then, COMMIT2 with ball & sticks forward model was used to filter the raw tractogram and compute the COMMIT2 weights of each streamline^{16,17}.

Voxel-based diffusion imaging analysis. The TBSS pipeline in FSL (version 6.0)³⁰ was used to compare MRI metric differences between the COV + and COV – groups (Fig. 4). The FA maps were nonlinearly aligned to the FMRIB-58 map in the template space of the Montreal Neuroimaging Institute (MNI). The FA skeleton mean was computed following the deformable registration. The FA maps deformation fields were utilized for FA, MD, RD, and AD. The registered maps were projected onto the FA skeleton.

Network construction. The brain network is composed of nodes and edges. To determine the nodes within the network, we selected 171 grey matter regions of the brain from the AAL3 atlas⁴⁶. Each AAL3 region in standard MNI space was back-transformed to the participant's native diffusion space. The COMMIT2-weighted tractogram and AAL3 parcellations were used to derive COMMIT2-weighted structural connectivity matrices (Fig. 4). The COMMIT2 weight of a streamline is a measure that quantifies the contribution to the diffusion MRI signal of each streamline and is proportional to the cross-sectional area of the biological fibers along their path. By its turn, the COMMIT2 weight of a connection corresponds to the sum of the individual weights assigned by COMMIT2 to each streamline connecting two parcels of the matrix and was used as a marker of connectivity strength. Through its ability to take into account the tracking bias related to variations in bundle width, the COMMIT2 weight constitutes a more biological proxy than the frequently used streamline count¹⁵. The possibility to inject priors about brain anatomy and its organization, and not only about microstructural properties, represents a powerful and novel way to tackle the false-positive problem in tractography and brain structural connectivity^{16,17}. COMMIT2-weighted 171 × 171 whole-brain matrices were computed.

Three-dimensional projections of structural connections and nodes were visualized using BrainNet Viewer (version 1.42)⁴⁷, for comparison of COMMIT2 weight matrices and graph theory analyses.

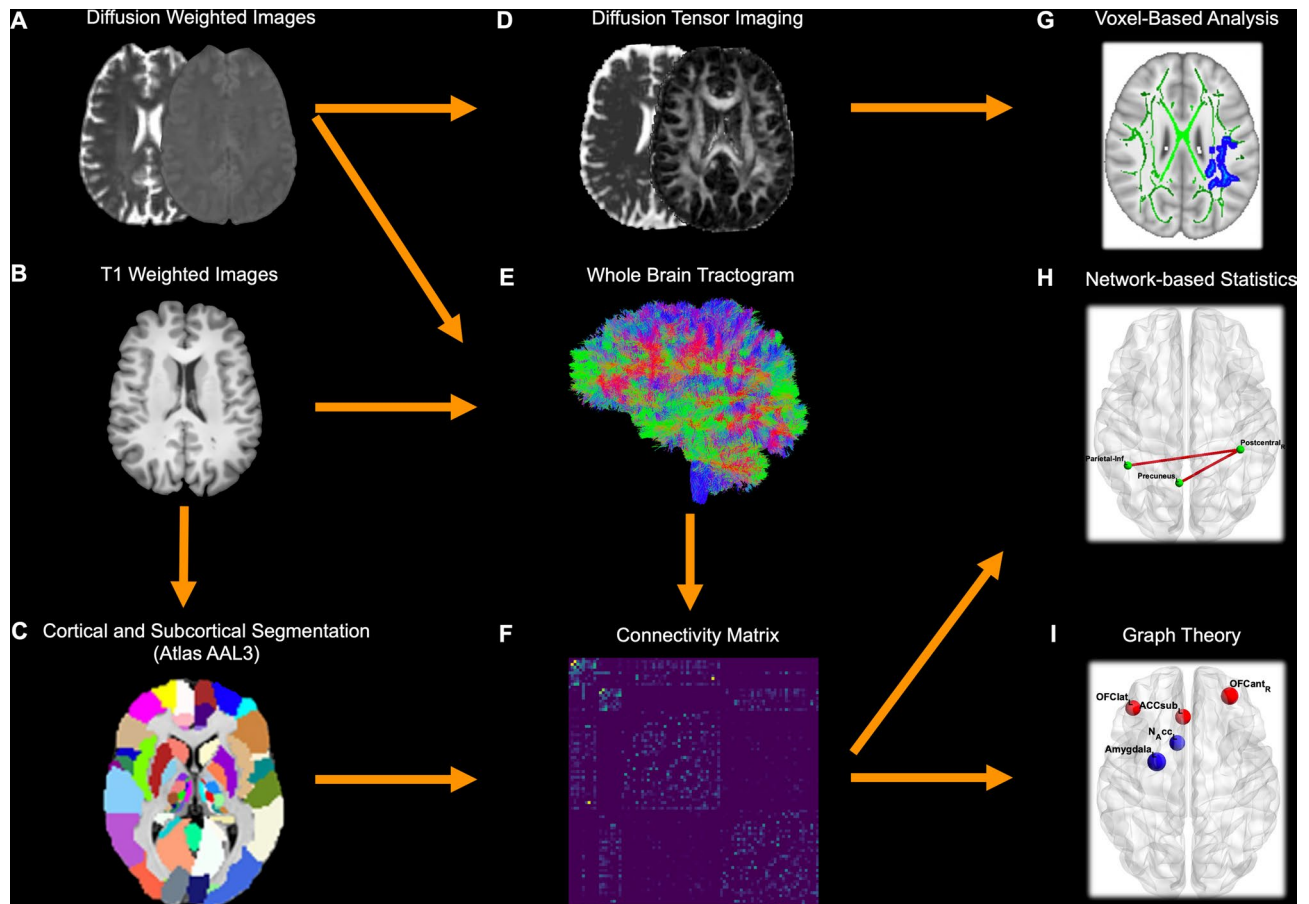


Figure 4. Processing flowchart. ((A) and (B)). The TractoFlow pipeline processes diffusion-weighted and T1-weighted images (C) T1-weighted images are labeled in 171 brain regions of the AAL3 atlas. (D) Diffusion MRI-derived measures are computed. (E) Whole brain probabilistic tractography is performed using an anatomically constrained particle filter algorithm. (F) Extraction of the COMMIT2-weighted connectivity matrix. (G) Voxel-based analysis investigated FA, MD, RD, and AD metrics. (H) Network-based statistics analysis. (I) Graph theory analysis: global and local network. AAL automated anatomical labeling, COMMIT convex optimization modeling for microstructure informed tractography, FA fractional anisotropy, MD mean diffusivity, RD radial diffusivity, AD axial diffusivity.

Network-based statistics. NBS was performed following Zalesky's methods with NBS Connectome (version 1.2) to determine the different connections^{48,49}. NBS is a statistical method based on graph theory and is often used to explore differences in the structural connectivity in the brain WM network. Typically, NBS analysis is conducted to identify subnetworks consisting of pairs of nodes and connections whose structural connectivity strength varies significantly between groups.

Network measures. The Brain Connectivity Toolbox (BCT) computed network measures for each subject⁵⁰. For global networks, betweenness centrality (corresponding to the fraction of all shortest paths in the network), modularity (reflecting the segregation of the network), assortativity (reflecting whether nodes tend to be connected to other nodes with similar strengths), participation (measure of diversity of intermodular connections), clustering coefficient (fraction of connected triangles around a node), mean strength (corresponding to the average of all the nodal strengths, where the nodal strength is the sum of the weights of links connected to the node), global efficiency (corresponding to the average inverse shortest path length in the network and inversely related to the characteristic path length), density (corresponding to the fraction of present connections to possible connections), characteristic path length (average of the shortest path length across all nodes), edge count, and small-worldness (ratio of average clustering coefficient to characteristic path length) were analyzed.

We analyzed regional network measures, calculated for each node, including betweenness centrality (number of shortest paths that pass through a node), clustering (fraction of connected triangles around a node), edge count, local efficiency (average of the inverse shortest path length in the neighborhood a node), nodal strength (sum of weights of links connected to the node), path length (shortest path length across the (average of the shortest path length across all nodes), and participation (a measure of the diversity of intermodular connections of a node).

Local network measures were calculated for the olfactory-related brain regions (olfactory cortex, gyrus rectus, medial orbital gyrus, anterior orbital gyrus, posterior orbital gyrus, lateral orbital gyrus, insula, hippocampus, parahippocampal gyrus, amygdala, caudate nucleus, putamen, pallidum, thalamus [mediodorsal medial nucleus and mediodorsal lateral nucleus], anterior cingulate cortex [subgenual, pregenual and supracallosal], and nucleus accumbens)^{51,52}.

MRI quality control. The MRI images were inspected for significant gross geometric distortion, mass movement, and signal drop artifacts to ensure their quality. For T1-weighted and dMRI images, a Nextflow pipeline for dMRI quality control (Dmriqc-flow) was also utilized⁵³.

Statistical analysis. *Demographic and clinical assessments.* The demographic and clinical characteristics of the groups were compared using independent-sample t-tests for normally distributed continuous variables, Mann–Whitney tests for nonnormally distributed continuous variables, and χ^2 for categorical variables. Fulfillment of the normality assumption was inspected through visual examination of variable distributions and the Shapiro–Wilk test. The significance level was set at $p < 0.05$. All statistical analyses were performed in R, version 4.1.0 (*R Foundation for Statistical Computing*, Vienna, Austria).

Segmentation of the olfactory bulbs. The olfactory bulb volumes were compared using a t-test for independent samples. To account for multiple comparisons, the results were adjusted using the False Discovery Rate (FDR) method⁵⁴. The eTIV corrected the volumes obtained with the formula: (volume of the olfactory bulb/eTIV) \times 100.

An analysis of covariance (ANCOVA) was performed to compare the normalized total olfactory bulb volume between groups, while controlling for variables such as sex, age, and allergic rhinosinusitis. As necessary, significant p-values were adjusted using post hoc Bonferroni tests ($p < 0.05$).

The level of interobserver agreement for the segmentation of the olfactory bulbs was assessed by the Pearson's correlation coefficient and the DSC. The DSC is an overlap similarity index that reflects agreement in size and location. It ranges from 0 (no overlap) to 1 (complete overlap) (Fig. 3). A satisfactory overlap exists when DSC > 0.70 ⁵⁵.

Voxel-based diffusion imaging analysis. To test for group differences, a general linear model (GLM) with contrast was performed on VBA data. The TBSS framework³⁰ includes nonparametric permutation testing (5000 permutations) to correct multiple comparisons and *threshold-free cluster enhancement* (TFCE). Age and sex were used as nuisance covariates. Results were considered significant at $p < 0.05$, TFCE corrected for multiple comparisons. WM regions were named according to the Johns Hopkins University white-matter tractography atlas.

Network-based statistics. Between-group differences (COV- $>$ COV+ and COV- $<$ COV+ contrasts) were tested on structural connectivity matrices for a range of primary thresholds (from $t = 2.5$ to $t = 3.5$), with age and sex as nuisance variables. Five thousand permutations were used, with intensity as the measure of network size and a statistical significance threshold set at $p < 0.05$.

Network metrics. Between-group differences were tested with either Mann–Whitney (modularity, clustering, and nodal strength) or independent-sample t-tests (other global network metrics). A GLM was used to analyze the local network metrics differences in olfactory-related brain areas between the control and COVID-19 groups, using age and sex as covariates. All results were corrected using the FDR method⁵⁴.

We performed a partial correlation analysis between global network measures, SS-16 test score, and normalized total olfactory bulb volume, adjusting for age, sex, education, comorbidities (allergic rhinosinusitis and migraine), and time between COVID-19 diagnosis and study clinical/imaging procedures. Data were analyzed using Spearman's coefficient. Statistical significance was defined as a two-tailed $p < 0.05$.

Data availability

The anonymized dataset that supports these study findings is available upon reasonable request from the corresponding author from a qualified investigator if the intent is to increase reproducibility. The data were not publicly available because of privacy or ethical restrictions.

Received: 30 March 2023; Accepted: 4 August 2023

Published online: 09 August 2023

References

1. COVID-19 Dashboard by the Center for Systems Science and Engineering (CSSE). Johns Hopkins University (JHU).
2. Al-Aly, Z., Xie, Y. & Bowe, B. High-dimensional characterization of post-acute sequelae of COVID-19. *Nature* **594**(7862), 259–264. <https://doi.org/10.1038/s41586-021-03553-9> (2021).
3. Nalbandian, A. *et al.* Post-acute COVID-19 syndrome. *Nat. Med.* **27**(4), 601–615. <https://doi.org/10.1038/s41591-021-01283-z> (2021).
4. Agyeman, A. A., Chin, K. L., Landersdorfer, C. B., Liew, D. & Ofori-Asenso, R. Smell and taste dysfunction in patients with COVID-19: A systematic review and meta-analysis. *Mayo Clin. Proc.* **95**(8), 1621–1631. <https://doi.org/10.1016/j.mayocp.2020.05.030> (2020).
5. Lechien, J. R. *et al.* Prevalence and 6-month recovery of olfactory dysfunction: A multicentre study of 1363 COVID-19 patients. *J. Intern Med.* **290**(2), 451–461. <https://doi.org/10.1111/joim.13209> (2021).

6. Sayin, İ, Yaşar, K. K. & Yazici, Z. M. Taste and smell impairment in COVID-19: An AAO-HNS anosmia reporting tool-based comparative study. *Otolaryngol. Neck Surg.* **163**(3), 473–479. <https://doi.org/10.1177/0194599820931820> (2020).
7. Xydakis, M. S. *et al.* Smell and taste dysfunction in patients with COVID-19. *Lancet Infect. Dis.* **20**(9), 1015–1016. [https://doi.org/10.1016/S1473-3099\(20\)30293-0](https://doi.org/10.1016/S1473-3099(20)30293-0) (2020).
8. Meinhardt, J. *et al.* Olfactory transmucosal SARS-CoV-2 invasion as a port of central nervous system entry in individuals with COVID-19. *Nat. Neurosci.* **24**(2), 168–175. <https://doi.org/10.1038/s41593-020-00758-5> (2021).
9. de Melo, G. D. *et al.* COVID-19-related anosmia is associated with viral persistence and inflammation in human olfactory epithelium and brain infection in hamsters. *Sci. Transl. Med.* <https://doi.org/10.1126/scitranslmed.abf8396> (2021).
10. Khan, M. *et al.* Visualizing in deceased COVID-19 patients how SARS-CoV-2 attacks the respiratory and olfactory mucosae but spares the olfactory bulb. *Cell* **184**(24), 5932–5949.e15. <https://doi.org/10.1016/j.cell.2021.10.027> (2021).
11. Brann, D. H. *et al.* Non-neuronal expression of SARS-CoV-2 entry genes in the olfactory system suggests mechanisms underlying COVID-19-associated anosmia. *Sci. Adv.* <https://doi.org/10.1126/sciadv.abc5801> (2020).
12. Ho, C.-Y. *et al.* Postmortem assessment of olfactory tissue degeneration and microvasculopathy in patients with COVID-19. *JAMA Neurol.* <https://doi.org/10.1001/jamaneurol.2022.0154> (2022).
13. Altunisik, E., Baykan, A. H., Sahin, S., Aydin, E. & Erturk, S. M. Quantitative analysis of the olfactory system in COVID-19: An MR imaging study. *AJNR Am. J. Neuroradiol.* **42**(12), 2207–2214. <https://doi.org/10.3174/ajnr.A7278> (2021).
14. Wingrove, J. *et al.* Aberrant olfactory network functional connectivity in people with olfactory dysfunction following COVID-19 infection: An exploratory, observational study. *EclinicalMedicine* **58**, 101883. <https://doi.org/10.1016/j.eclinm.2023.101883> (2023).
15. Yeh, C.-H., Jones, D. K., Liang, X., Descoteaux, M. & Connelly, A. Mapping structural connectivity using diffusion MRI: Challenges and opportunities. *J Magn. Reson. Imaging* **53**(6), 1666–1682. <https://doi.org/10.1002/jmri.27188> (2021).
16. Daducci, A., Dal Palù, A., Lemkaddem, A. & Thiran, J.-P. COMMIT: Convex optimization modeling for microstructure informed tractography. *IEEE Trans. Med. Imaging* **34**(1), 246–257. <https://doi.org/10.1109/TMI.2014.2352414> (2015).
17. Schiavi, S. *et al.* A new method for accurate in vivo mapping of human brain connections using microstructural and anatomical information. *Sci. Adv.* **6**(31), eaba8245. <https://doi.org/10.1126/sciadv.aba8245> (2020).
18. Zhang, F. *et al.* Quantitative mapping of the brain's structural connectivity using diffusion MRI tractography: A review. *Neuroimage* **249**, 118870. <https://doi.org/10.1016/j.neuroimage.2021.118870> (2022).
19. Dan, X. *et al.* Olfactory dysfunction in aging and neurodegenerative diseases. *Ageing Res Rev.* **70**, 101416. <https://doi.org/10.1016/j.arr.2021.101416> (2021).
20. Chen, B. *et al.* Aberrancies of brain network structures in patients with anosmia. *Brain Topogr.* **33**(3), 403–411. <https://doi.org/10.1007/s10548-020-00769-2> (2020).
21. Sreenivasan, K. *et al.* Olfactory network differences in master sommeliers: Connectivity analysis using granger causality and graph theoretical approach. *Brain Connect.* **7**(2), 123–136. <https://doi.org/10.1089/brain.2016.0458> (2017).
22. Hummel, T., Kobal, G., Gudziol, H. & Mackay-Sim, A. Normative data for the “Sniffin” Sticks” including tests of odor identification, odor discrimination, and olfactory thresholds: An upgrade based on a group of more than 3,000 subjects”. *Eur. Arch. Oto-Rhino-Laryngol.* **264**(3), 237–243. <https://doi.org/10.1007/s00405-006-0173-0> (2007).
23. Altundag, A. *et al.* Olfactory cleft measurements and COVID-19-related anosmia. *Otolaryngol. Neck Surg. Off. J. Am. Acad. Otolaryngol. Neck Surg.* **164**(6), 1337–1344. <https://doi.org/10.1177/0194599820965920> (2021).
24. Hoffmann, M. *et al.* SARS-CoV-2 cell entry depends on ACE2 and TMPRSS2 and is blocked by a clinically proven protease inhibitor. *Cell* **181**(2), 271–280.e8. <https://doi.org/10.1016/j.cell.2020.02.052> (2020).
25. Butowt, R. & von Bartheld, C. S. Anosmia in COVID-19: Underlying mechanisms and assessment of an olfactory route to brain infection. *Neurosci. Rev. J. Bringing Neurobiol. Neurol. Psychiatry* **27**(6), 582–603. <https://doi.org/10.1177/1073858420956905> (2021).
26. Hummel, T., Sekinger, B., Wolf, S. R., Pauli, E. & Kobal, G. “Sniffin” sticks: olfactory performance assessed by the combined testing of odor identification, odor discrimination and olfactory threshold. *Chem. Senses.* **22**(1), 39–52. <https://doi.org/10.1093/chemse/22.1.39> (1997).
27. Silveira-Moriyama, L. *et al.* The use of smell identification tests in the diagnosis of Parkinson's disease in Brazil. *Mov. Disord.* **23**(16), 2328–2334. <https://doi.org/10.1002/mds.22241> (2008).
28. Tan, C.J.-W. *et al.* Neuroradiological basis of COVID-19 olfactory dysfunction: A systematic review and meta-Analysis. *Laryngoscope* **132**(6), 1260–1274. <https://doi.org/10.1002/lary.30078> (2022).
29. Buschhüter, D. *et al.* Correlation between olfactory bulb volume and olfactory function. *Neuroimage* **42**(2), 498–502. <https://doi.org/10.1016/j.neuroimage.2008.05.004> (2008).
30. Smith, S. M. *et al.* Tract-based spatial statistics: Voxelwise analysis of multi-subject diffusion data. *Neuroimage* **31**(4), 1487–1505. <https://doi.org/10.1016/j.neuroimage.2006.02.024> (2006).
31. Douaud, G. *et al.* SARS-CoV-2 is associated with changes in brain structure in UK Biobank. *Nature* **604**(7907), 697–707. <https://doi.org/10.1038/s41586-022-04569-5> (2022).
32. Rau, A. *et al.* Widespread white matter oedema in subacute COVID-19 patients with neurological symptoms. *Brain* <https://doi.org/10.1093/brain/awac045> (2022).
33. Pelizzari, L. *et al.* Mid-term MRI evaluation reveals microstructural white matter alterations in COVID-19 fully recovered subjects with anosmia presentation. *Ther. Adv. Neurol. Disord.* **15**, 1756286422111996. <https://doi.org/10.1177/1756286422111996> (2022).
34. Bispo, D. *et al.* Brain microstructural changes and fatigue after COVID-19. *Front. Neurol.* <https://doi.org/10.3389/fneur.2022.1029302> (2022).
35. Irvani, B. *et al.* Acquired olfactory loss alters functional connectivity and morphology. *Sci. Rep.* **11**(1), 16422. <https://doi.org/10.1038/s41598-021-95968-7> (2021).
36. Zhang, H., Chung, T.W.-H., Wong, F.K.-C., Hung, I.F.-N. & Mak, H.K.-F. Changes in the intranetwork and internetwork connectivity of the default mode network and olfactory network in patients with COVID-19 and olfactory dysfunction. *Brain Sci.* <https://doi.org/10.3390/brainsci12040511> (2022).
37. Esposito, F. *et al.* Olfactory loss and brain connectivity after COVID-19. *Hum. Brain Mapp.* **43**(5), 1548–1560. <https://doi.org/10.1002/hbm.25741> (2022).
38. NeuroCOVID-19. Brazilian Registry NeuroCovBr. <https://www.neurocovbr.com/>. Accessed 1 February 2022.
39. Cesar, K. G., Yassuda, M. S., Porto, F. H. G., Brucki, S. M. D. & Nitrini, R. MoCA Test: Normative and diagnostic accuracy data for seniors with heterogeneous educational levels in Brazil. *Arq. Neuropsiquiatr.* **77**(11), 775–781. <https://doi.org/10.1590/0004-282X20190130> (2019).
40. Nasreddine, Z. S. *et al.* The Montreal Cognitive Assessment, MoCA: A brief screening tool for mild cognitive impairment. *J. Am. Geriatr. Soc.* **53**(4), 695–699. <https://doi.org/10.1111/j.1532-5415.2005.53221.x> (2005).
41. Yushkevich, P. A. *et al.* User-guided 3D active contour segmentation of anatomical structures: Significantly improved efficiency and reliability. *Neuroimage* **31**(3), 1116–1128. <https://doi.org/10.1016/j.neuroimage.2006.01.015> (2006).
42. Paschen, L. *et al.* The olfactory bulb volume in patients with idiopathic Parkinson's disease. *Eur. J. Neurol.* **22**(7), 1068–1073. <https://doi.org/10.1111/ene.12709> (2015).
43. Theaud, G. *et al.* TractoFlow: A robust, efficient and reproducible diffusion MRI pipeline leveraging Nextflow & Singularity. *Neuroimage* **218**, 116889. <https://doi.org/10.1016/j.neuroimage.2020.116889> (2020).
44. Girard, G., Whittingstall, K., Deriche, R. & Descoteaux, M. Towards quantitative connectivity analysis: Reducing tractography biases. *Neuroimage* **98**, 266–278. <https://doi.org/10.1016/j.neuroimage.2014.04.074> (2014).

45. Scilpy. Sherbrooke Connectivity Imaging Lab. <https://github.com/scilus/scilpy>. Accessed 1 February 2022.
46. Rolls, E. T., Huang, C.-C., Lin, C.-P., Feng, J. & Joliot, M. Automated anatomical labelling atlas 3. *Neuroimage*. **206**, 116189. <https://doi.org/10.1016/j.neuroimage.2019.116189> (2020).
47. BrainNet Viewer. <https://www.nitrc.org/projects/bnv/>. Accessed 1 February 2022.
48. Zalesky, A., Fornito, A. & Bullmore, E. T. Network-based statistic: Identifying differences in brain networks. *Neuroimage* **53**(4), 1197–1207. <https://doi.org/10.1016/j.neuroimage.2010.06.041> (2010).
49. Network Based Statistic Toolbox. <https://sites.google.com/site/bctnet/network-based-statistic-toolbox>. Accessed 1 February 2022.
50. Rubinov, M. & Sporns, O. Complex network measures of brain connectivity: Uses and interpretations. *Neuroimage* **52**(3), 1059–1069. <https://doi.org/10.1016/j.neuroimage.2009.10.003> (2010).
51. Han, P., Zang, Y., Akshita, J. & Hummel, T. Magnetic resonance imaging of human olfactory dysfunction. *Brain Topogr.* **32**(6), 987–997. <https://doi.org/10.1007/s10548-019-00729-5> (2019).
52. Seubert, J., Freiherr, J., Djordjevic, J. & Lundström, J. N. Statistical localization of human olfactory cortex. *Neuroimage* **66**, 333–342. <https://doi.org/10.1016/j.neuroimage.2012.10.030> (2013).
53. A Nextflow pipeline for diffusion MRI quality check (dmriqc_flow). Sherbrooke Connectivity Imaging Lab. https://github.com/scilus/dmriqc_flow. Accessed 1 February 2022.
54. Benjamini, Y. & Hochberg, Y. Controlling the false discovery rate: A practical and powerful approach to multiple testing. *J. R. Stat. Soc. Ser. B* **57**(1), 289–300. <https://doi.org/10.1111/j.2517-6161.1995.tb02031.x> (1995).
55. Zijdenbos, A. P., Dawant, B. M., Margolin, R. A. & Palmer, A. C. Morphometric analysis of white matter lesions in MR images: Method and validation. *IEEE Trans. Med. Imaging* **13**(4), 716–724. <https://doi.org/10.1109/42.363096> (1994).

Acknowledgements

The authors thank the patients and controls for their participation in the study. We would like to thank the staff of Hospital Santa Marta for their assistance in collecting the MRI data. We also thank the Sherbrooke Connectivity Imaging Lab team for their assistance, guidance, and cooperation in the MRI data processing.

Author contributions

D.B., P.B., D.P., F.G., A.S. and N.R.: study design. D.B., P.B., D.P., M.D. and N.R.: analysis and interpretation of data. D.B., P.B. and D.P.: drafting of the manuscript. D.B., P.B., D.P., F.M., B.D., H.P., F.G., A.O., N.R., A.S. and M.D.: critical revision of the manuscript.

Competing interests

The authors declare no competing interests.

Additional information

Supplementary Information The online version contains supplementary material available at <https://doi.org/10.1038/s41598-023-40115-7>.

Correspondence and requests for materials should be addressed to D.D.C.B.

Reprints and permissions information is available at www.nature.com/reprints.

Publisher's note Springer Nature remains neutral with regard to jurisdictional claims in published maps and institutional affiliations.



Open Access This article is licensed under a Creative Commons Attribution 4.0 International License, which permits use, sharing, adaptation, distribution and reproduction in any medium or format, as long as you give appropriate credit to the original author(s) and the source, provide a link to the Creative Commons licence, and indicate if changes were made. The images or other third party material in this article are included in the article's Creative Commons licence, unless indicated otherwise in a credit line to the material. If material is not included in the article's Creative Commons licence and your intended use is not permitted by statutory regulation or exceeds the permitted use, you will need to obtain permission directly from the copyright holder. To view a copy of this licence, visit <http://creativecommons.org/licenses/by/4.0/>.

© The Author(s) 2023